Available online at www.sciencedirect.com
ScienceDirect
Journal of Power Sources 173 (2007) 681–687
JOURNAL OF POWER SOURCES
www.elsevier.com/locate/jpowsour

Structural, electrical and transport properties of yttrium-doped proton-conducting strontium cerates

P. Pasierb *, M. Wierzbicka, S. Komornicki, M. Rekas

AGH University of Science and Technology, Faculty of Materials Science and Ceramics, al. Mickiewicza 30, 30-059 Krakow, Poland

Available online 21 May 2007

Abstract

Series of $SrCe_{1-x}Y_xO_{3-\delta}$ solid solutions with x varying between 0 and 0.2 were prepared by solid-state reaction method. XRD results revealed that samples with $0 \leq x < 0.1$ ($SrCe_{1-x}Y_xO_{3-\delta}$) are homogenous perovskite phases, while the samples with higher concentration of yttrium contain admixture of other phase (identified as Sr_2CeO_4). According to SEM observations the samples were dense with uniform grain sizes within 3–5 μm. Impedance spectroscopic investigations revealed a strong influence of Y concentration on electrical properties of $SrCe_{1-x}Y_xO_{3-\delta}$. The activation energies of the total electrical conductivity as well as grain boundary and bulk components have been determined. Mixed ionic-electronic conductivity in studied materials at experimental conditions has been observed. Potentiometric measurements of EMF versus temperature of solid cells containing studied materials as solid electrolytes were performed in order to determine ionic transference numbers versus temperature.

Keywords: Protonic conductors; Strontium cerium oxides; Impedance spectroscopy; Transference numbers

1. Introduction

In early 1980s Iwahara et al. [1] found several perovskite-type oxides exhibiting high proton conductivity at elevated temperatures, above 450 °C. Typical examples of this class of materials, called as high temperature protonic conductors, are barium and strontium cerates doped with rare earth elements. The conductivity of some members of this family (e.g. $BaCeO_3$) can reach the value of the order of 10^{-2} S cm^{-1} [2].

Two different mechanisms of proton defects movement have been proposed. First of them assumes proton transfer between neighboring oxygen ions and reorientation of the hydroxide ion on the oxygen site (Grotthuss mechanism) [3]. According to both experimental studies [4,5] and numerical simulations [6,7] the reorientation step is much faster than proton transfer. According to this mechanism the proton is the only mobile species while the oxygen is localized in the vicinity of its lattice position. Second mechanism termed as 'vehicle mechanism' assumes transport of protons by other species, e.g. by oxygen ions. This mechanism is usually restricted to materials with open structures (channels, layers) enabling movement of large ions and molecules [2].

Apart from both mentioned transport mechanisms, there is a hypothesis on presence of free protons in solid oxide [8,9] capable of moving through the material; however there are no experimental data which confirms this hypothesis.

High temperature protonic conductors can be used in various practical areas such as hydrogen-containing gas sensors, fuel cells, hydrogen pumps and membranes, which usually work in the range of 400–600 °C. According to the generally accepted model, protonic defects are formed in perovskite structure due to incorporation of either water or hydrogen molecules from the gas phase. These reactions are facilitated by presence of point defects in crystal lattice such as oxygen vacancies, $V_O^{\bullet\bullet}$. Undoped $SrCeO_3$ exhibits only low electrical conductivity [10,11], due to low point defects concentrations, mainly oxygen vacancies resulting from the interaction of the crystal with gas phase [12]. The concentration of oxygen vacancies in perovskite oxides can be considerably increased (and in controlled way) by acceptor doping. So, in order to obtain higher values of oxygen vacancy concentrations, $[V_O^{\bullet\bullet}]$, and resulting higher concentration of protonic defects, the acceptor doping is needed. Rare earth elements such as Yb, Gd, Nd and Y are usually used as dopants in case of barium and strontium cerates [13].

Annealing of acceptor-doped material, $SrCe_{1-x}Y_xO_{3-\delta}$, in water vapor [10,14,15] or in a hydrogen-containing atmosphere [8,14,16–18] leads to the formation of protonic defects. The

* Corresponding author. Tel.: +48 12 617 25 33; fax: +48 12 617 24 93.
E-mail address: ppasierb@uci.agh.edu.pl (P. Pasierb).

0378-7753/$ – see front matter © 2007 Elsevier B.V. All rights reserved.
doi:10.1016/j.jpowsour.2007.05.057

formation of protonic defects in $SrCeO_3$-based material may change its electrical and ionic transport properties. The protonic defects can take part in electrical conductivity of the material.

The protonic conductivity increases with acceptor dopant concentration in either Ba- or Sr-cerates, however solubility of typical acceptor dopants such as Y_2O_3 in perovskite lattice is limited. In literature there are no agreements concerning the solubility of acceptor-type oxides in Ba- or Sr-cerates [16].

The purpose of this work was to investigate the influence of yttrium dopant concentration (x) on the phase composition, structure, microstructure, and some electrical properties of $SrCe_{1-x}Y_xO_{3-\delta}$ compounds. In particularly determination of the solubility Y_2O_3 in $SrCeO_3$ crystal lattice and the electrical properties of the saturated $SrCe_{1-x}Y_xO_{3-\delta}$ solid solutions was the aim of this paper.

2. Experimental

2.1. Materials preparation

Powders of $SrCe_{1-x}Y_xO_{3-\delta}$ ($x = 0.0$, 0.01, 0.025, 0.05, 0.1 and 0.2) were prepared by solid-state reaction method. Strontium carbonate $SrCO_3$ (99.9%, Johnson Matthey, Materials Technology, UK), cerium(IV) oxide CeO_2 (99.9%, Aldrich Chemical Company, Inc.) were used as starting materials. Yttrium dopant was introduced by impregnation of starting powders mixture with the water solution of yttrium(III) nitrate(V) (0.065 g of Y_2O_3 in 1 cm^3 of solution). The yttrium(III) nitrate(V) hexahydrate, $Y(NO_3)_3{\cdot}6H_2O$, (99.9%, Aldrich Chemical Company, Inc.) was used for preparation of the solution. After mixing of appropriate amounts of starting powders and impregnation the materials were dried at 80 °C and calcined at 1175 °C for 12 h. The reaction of formation of strontium cerium oxide can be written as follows:

$$SrCO_3 + (1-x)CeO_2 + xY(NO_3)_3{\cdot}6H_2O \Leftrightarrow SrCe_{(1-x)}Y_xO_{3-x/2} + CO_2\uparrow + 3xNO_2 + 6xH_2O + 3/4xO_2 \quad (1)$$

The obtained materials were crushed in agate mortar, milled, then formed in pellet die (Ø = 13 mm) at 37 MPa, isostatically pressed at 250 MPa and sintered at 1500 °C for 12 h.

Prior to electrical measurements porous Pt electrodes were applied at both sides of every pellet (Demetron Pt paste fired at 850 °C/5 min). Additionally, the pellets of solid electrolytes designated for determination of transference numbers, after application of Pt porous electrodes, were attached to alumina tubes (o.d. = 8 mm, i.d. = 5 mm) using the Ceramabond 569 ceramic adhesive.

All obtained pellets of solid electrolytes were stored in dessicator until used in further tests and experiments.

2.2. Experimental methods

In this work, the X-ray Diffraction (XRD), scanning electron microscopy (SEM), electrochemical impedance spectroscopy (EIS) and the measurements of electromotive force of electrochemical cells were used to characterize the obtained materials.

XRD measurements were done using Cu Kα filtered radiation (Philips X'Pert) within the 2θ range 10–90° with the scan rate of 0.008° s^{-1}. The lattice parameters were calculated using X'Pert+ (Philips) software according to the Rietveld method [19].

The SEM observations were done using JEOL JSM-5400 scanning electron microscope. The microphotographs were done at different magnifications 2000× to 5000× on freshly prepared fractures, sputtered by thin layer of carbon.

The impedance measurements were performed using a Frequency Response Analyser, Solartron, model 1260 coupled with the Solartron Dielectric Interface, 1296. The measurements were done in typical sample holder allowing the control of temperature and gas atmosphere composition. The amplitude of the sinusoidal voltage signal was 20 mV. The impedance spectra were recorded in the frequency range of 0.1 Hz–1 MHz, in the temperature range 830–1000 K and pO_2 of 10^{-15}–10^4 Pa, using O_2 (synthetic air), Ar and Ar/H_2 (7 vol.%) mixtures. The required gas composition was obtained by mixing the gas mixtures at proper ratio, using the MKS gas flow controllers. Prior to each measurement each sample was equilibrated at least 2 h at steady conditions. The quantitative values of the equivalent circuit components were derived using the ZPLOT software supplied with the Solartron system.

Potentiometric measurements of EMF versus temperature of solid cells build from studied materials as solid electrolytes were performed in sample holder allowing the delivery of different gas atmospheres at both sides of the cells. The temperature and oxygen partial pressure ranges applied were the same as in the case of EIS measurements, described above.

3. Results and discussion

3.1. Structure and phase composition

Fig. 1 shows the XRD measurements of $SrCe_{1-x}Y_xO_{3-\delta}$ pellets after sintering at 1500 °C for 12 h, as a function of Y dopant concentration (x). The magnification of narrow range of 2θ angle for samples with $x = 0.05$, 0.1 and 0.2 is shown in the inset. Basing on XRD results it can be stated that that samples with $0 \le x \le 0.05$ ($SrCe_{1-x}Y_xO_{3-\delta}$) crystallize only in perovskite structure, while the samples with higher concentration ($x = 0.1$ and 0.2) of yttrium dopant contain admixture of other phase. The additional phase was found to be probably the Sr_2CeO_4. The obtained results are in general agreement with the results presented in [13] where the solubility limit (lower than 20%) of rare earth element in this group of materials was defined.

Fig. 2 shows the derived lattice parameters. The observed changes of lattice parameters with yttrium content indicate the complex mechanism of incorporation of yttrium in crystallographic structure. The decrease of lattice parameters may be related to the formation of oxygen vacancies responsible for the shrinkage of the lattice. The parameter a shows the remarkable changes with yttrium content. Assuming this dependence

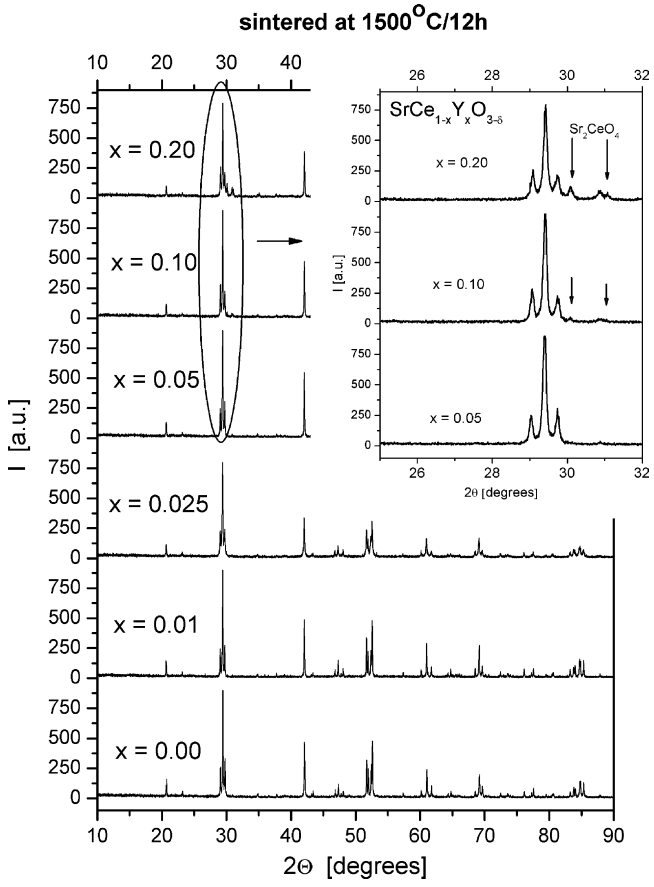

Fig. 1. The results of XRD measurements of $SrCe_{1-x}Y_xO_{3-\delta}$ pellets after sintering at 1500 °C for 12 h, as a function of yttrium dopant concentration (x). The magnification for narrow 2θ angle range in case of samples with $x = 0.05$, 0.1 and 0.2 is shown in the inset.

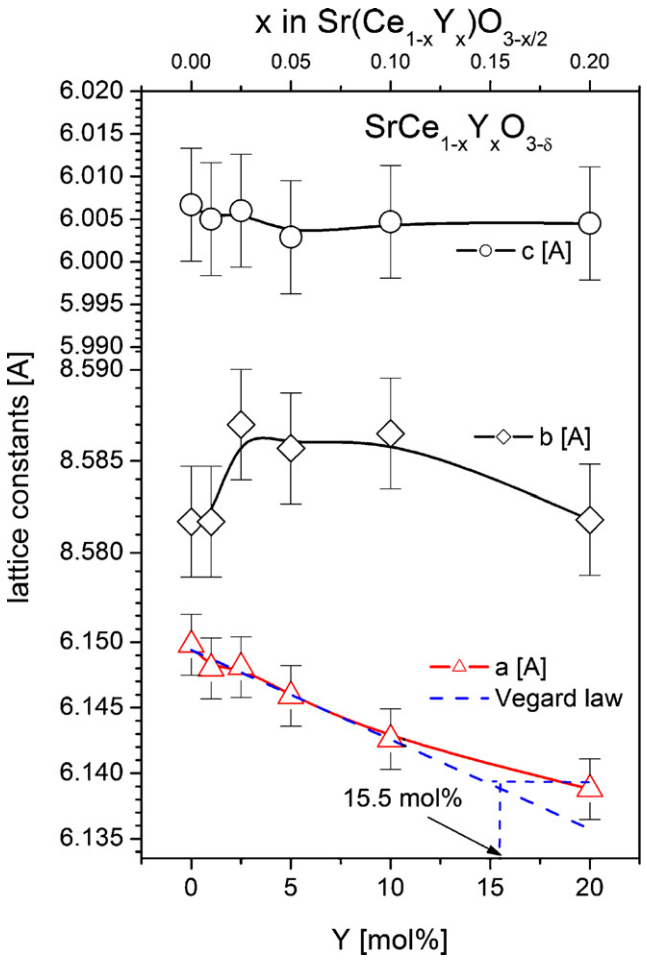

Fig. 2. The lattice parameters a, b, and c as a function of yttrium dopant concentration, x, derived from XRD data using Rietveld method [19].

as linear (i.e. Vegard's law, dashed line in Fig. 2) within perovskite phase stability, the determined maximum concentration of yttrium (solubility of yttria in perovskite lattice) is about (15.5 ± 1.9) mol.%. From the other hand the results presented in Fig. 1, where the additional reflexes for samples with $x = 0.10$ and 0.20 were detected, suggest lower solubility limit of Y in the lattice. Changes of a lattice parameter observed in this paper are in general agreement with the results presented in [20], where the monotonic decrease of calculated unit cell volume with increase of yttrium dopant contents was observed, but different interpretation was proposed. Namely, according to Philips et al. [20] the observed variation of unit cell volume with yttrium content could be due to ordering of the Y-dopant or could be due to substitution of a small amount of Y in the Sr sublattice.

3.2. Microstructure

Fig. 3 shows the SEM microphotographs of fractured $SrCe_{1-x}Y_xO_{3-\delta}$ pellets sintered at 1500 °C for 12 h, as a function of x, for two different magnifications (2000× and 5000×). SEM observations have proven that dense materials exhibiting uniform grain sizes were obtained in the case of all compositions. The estimated overage grain size was found to be in the range of 3–5 μm, almost independently on composition. Slight decrease of porosity and some traces of glassy phase with increase of yttrium dopant concentration can be observed. The regions with different morphology were found in the case of samples with $x \geq 0.1$, which can be attributed to the presence of additional phase.

3.3. Electrical properties

Fig. 4A–C present the representative results of the impedance plots $-Z''$ versus Z' (where Z'' and Z' describe imaginary and real parts of impedance, respectively) as a function of temperature (graph A for $SrCeO_{3-\delta}$ and graph B for $SrCe_{0.8}Y_{0.2}O_{3-\delta}$) and as a function of oxygen partial pressure (graph C, for $SrCe_{0.8}Y_{0.2}O_{3-\delta}$). Generally, two semicircular parts may be distinguished. It is commonly accepted that the high-frequency part of the spectrum corresponds to the bulk of solid electrolyte while second part (semicircle) is related to a partial blocking of oxygen ions at the internal surfaces of the electrolyte such as grain boundaries, insulating inclusions of impurities and other microstructure defects like pores and cracks. The third, if observed, characterize electrode reactions. In order to analyse quantitatively observed spectra we have chosen an equivalent circuit composed of resistor $R_{electrode}$ and two parallel R_i–CPE_i

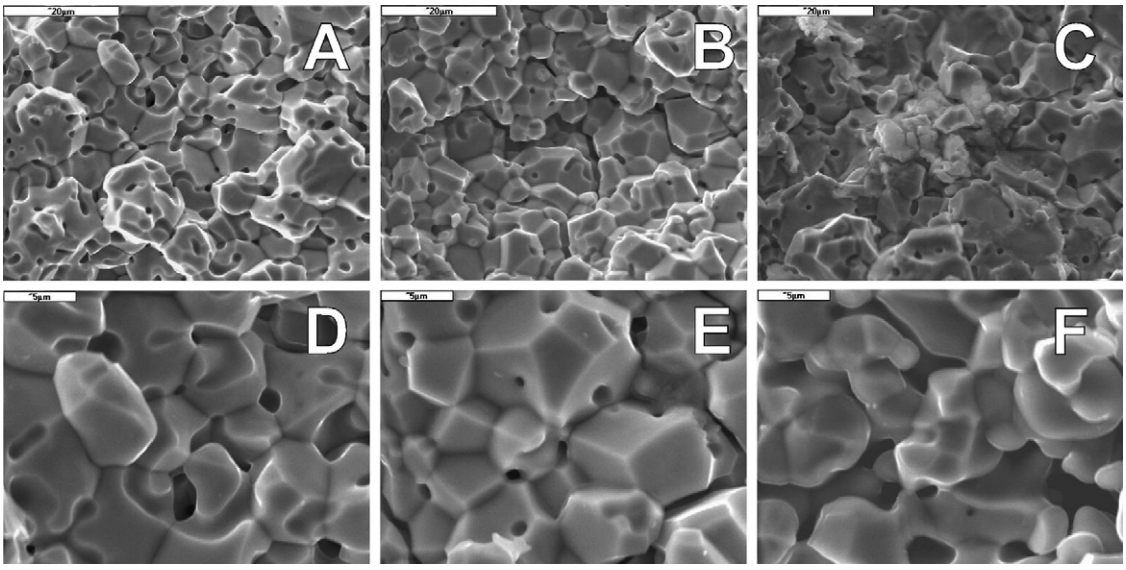

Fig. 3. SEM microphotographs of fractured $SrCe_{1-x}Y_xO_{3-\delta}$ pellets sintered at 1500 °C for 12 h, as a function of x, for two different magnifications (upper row, 2000× and lower row, 5000×). $x = 0.00$ (A and D), $x = 0.05$ (B and E) and $x = 0.20$ (C and F).

(constant phase angle element) sub-circuits in series, corresponding to the bulk and grain boundary properties.

According to the presented micrographs in Fig. 3, the additional Sr_2CeO_4 phase is in the minority and is not continuous, so its effect on electrical properties may be neglected in this case.

Electrical conductivities σ_b and σ_{gb} were determined from the first (high-frequency) and second (intermediate-frequency) parts of the spectra, respectively, presented in Fig. 4A–C. The most interesting results (corresponding to the low pO_2 pressure range) were collected in Fig. 5 as $\log(\sigma T)$ versus T^{-1}, and the activation energies were determined. As can be seen the determined electrical conductivity of grain boundaries assumes higher activation energy than those of bulk conductivity. This relation was found to be independent on composition (as shown in this figure), and also not dependent on oxygen partial pressure. Additionally, the results presented in Fig. 5 indicate the strong influence of yttrium dopant on the activation energy of grain boundary conductivity.

Activation energy of grain boundaries remains higher than that of the bulk. This fact is commonly observed for ceramic materials generally [21] and for cerate perovskites particularly [22]. However, in case of undoped sample ($x = 0.00$) the differences between the activation energies of grain boundary and bulk are much higher than that for doped sample ($x = 0.20$). This fact may result from higher contribution of electronic conductivity in total electrical conductivity in case of undoped sample than that in doped one [22] (activation energies of both electron and electron holes conductivity are higher than ionic conductivity, Ref. 1 & 9 in [22]).

Fig. 6 shows the typical dependence of total electrical conductivity on oxygen partial pressure, shown as $\log\sigma$ versus $\log(pO_2)$ for isothermal conditions. Three different pO_2 regions can be distinguished, corresponding to different conduction mechanisms. At low oxygen partial pressure the oxygen exponent $1/n$ in the relation $\sigma \sim pO_2^{1/n}$ assumes value close to $-1/4$, which corresponds to the dominance of electron as a carrier. At intermediate pO_2 pressure range the independent conductivity region is observed which corresponds to ionic conductivity. At high oxygen partial pressure the oxygen exponent $1/n$ in the relation $\sigma \sim pO_2^n$ assumes value of $\approx 1/4$, which corresponds to the dominance of holes as a carrier. These results are in general agreement with the results presented previously [17,21] and the defect structure model presented in theoretical part.

3.4. Transference numbers

In order to determine the transference numbers of oxygen vacancies and protonic defect the potentiometric EMF measurements of different electrochemical cells were performed. Namely, the open cell voltage, $E_.$, of following cells was measured as a function of temperature:

$$\mathrm{Pt}, p(\mathrm{X_2})^{(1)}, p(\mathrm{H_2O})^{(1)} | \mathrm{SrCe_{1-x}Y_xO_{3-\delta}} | p(\mathrm{X_2})^{(2)}, p(\mathrm{H_2O})^{(2)}, \mathrm{Pt} \quad (2)$$

where $p(X_2)^{(1)}$ and $p(X_2)^{(2)}$ describe the hydrogen or oxygen atmosphere with defined pressures at both sides of the cells.

The open cell voltage, E, of the concentration cell (2) exposed to different gases at electrodes (1) and (2) can be expressed as [22]:

$$E = -\frac{1}{F}\sum_i \int_1^2 \frac{t_i}{z_i}\, \mathrm{d}\mu_{x_2} \quad (3)$$

where t_i and z_i are transference number and charge of defect 'i', respectively; μ_{X_2} is chemical potential of the gas X_2:

$$\mu_{x_2} = 2\eta_X + z_x\eta_e \quad (4)$$

where η_x and η_e are the electrochemical potentials of the ions X and electrons (Fermi energy), respectively.

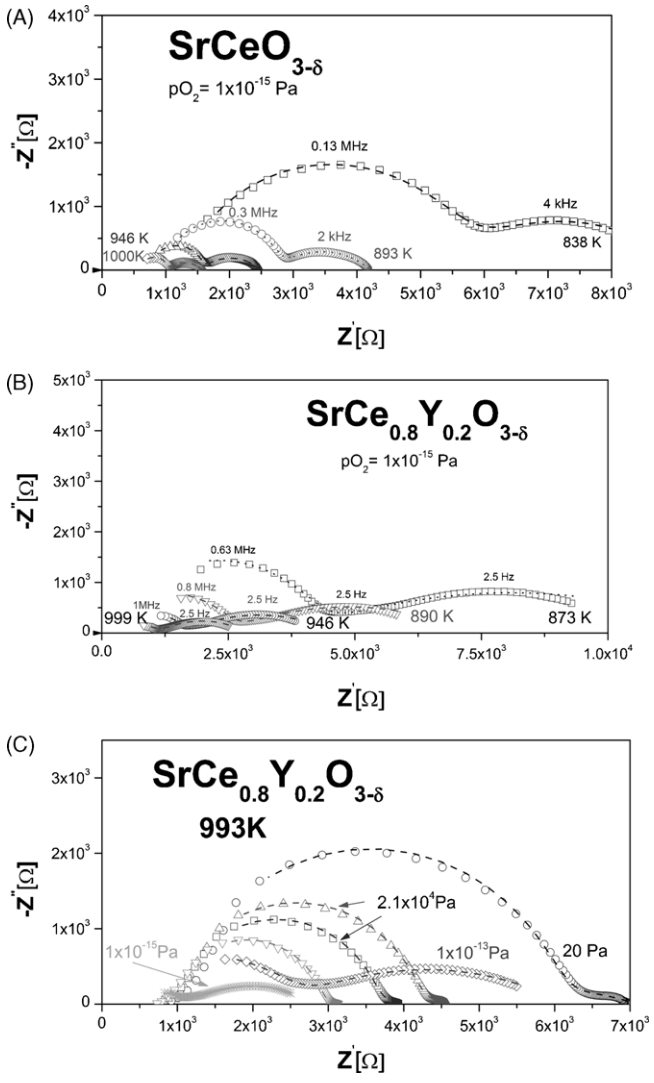

Fig. 4. Impedance plots $-Z''$ vs. Z' measured for different temperatures (graph A for $SrCeO_{3-\delta}$ and graph B for $SrCe_{0.8}Y_{0.2}O_{3-\delta}$) and different oxygen partial pressures (graph C, shown for $SrCe_{0.8}Y_{0.2}O_{3-\delta}$).

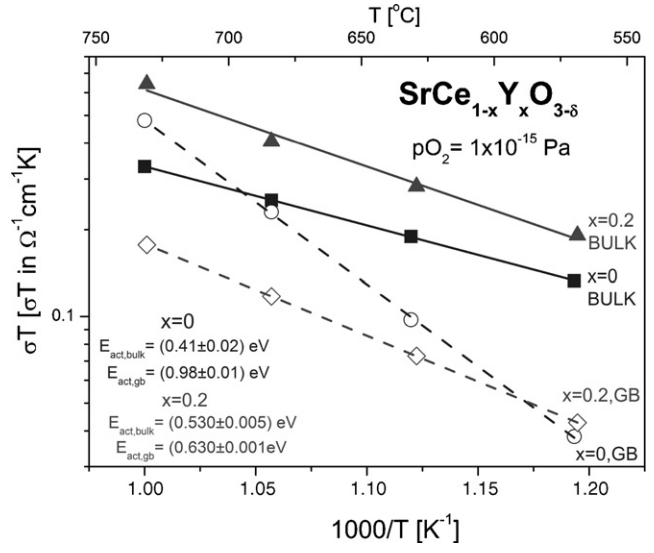

Fig. 5. The $\log(\sigma T)$ vs. T^{-1} plot or determined for the low pO_2 pressure range for undoped ($x = 0.00$) and doped ($x = 0.20$) samples.

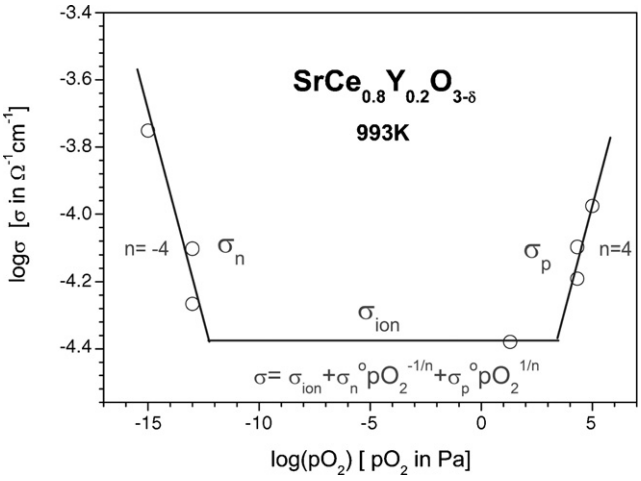

Fig. 6. Typical dependence of total electrical conductivity on oxygen partial pressure, shown as $\log\sigma$ vs. $\log(pO_2)$ for isothermal conditions ($T = 993$ K).

3.4.1. Cells containing O_2 and H_2O in both (1) and (2) gas atmospheres

If gas atmosphere at electrodes contain oxygen (i.e. the $X_2 = O_2$ in the Eq. (2)) and water vapor, the electrode reactions include:

$$\tfrac{1}{2}\,O_{2(g)} + 2e^- \Leftrightarrow O^{2-} \tag{5}$$

$$H_2O_{(g)} \Leftrightarrow 2H^+ + \tfrac{1}{2}O_{2(g)} + 2e^- \tag{6}$$

After integration of Eq. (3) we get:

$$E = \frac{RT}{4F}(t_O + t_H)\,\ln\frac{pO_2^{(2)}}{pO_2^{(1)}} - \frac{RT}{2F}t_H\,\ln\frac{pH_2O^{(2)}}{pH_2O^{(1)}} \tag{7}$$

Taking into account that in our experiments:

$$pH_2O^{(1)} = pH_2O^{(2)} \tag{8}$$

The Eq. (7) assumes the form:

$$E = \frac{RT}{4F}(t_O + t_H)\ln\frac{pO_2^{(2)}}{pO_2^{(1)}} \tag{9}$$

It means that the measurement of E leads to the determination of the total ionic transference numbers ($t_O + t_H$).

The dependence of E as a function of pO_2 at 873 K for $SrCeO_3$ solid electrolyte is illustrated Fig. 7. The ionic transference numbers ($t_O + t_H$) were determined from the linear approximation of the experimental points.

3.4.2. Cells containing H_2 and H_2O in both (1) and (2) gas atmospheres

If gas atmospheres at electrodes contain hydrogen (i.e. the $X_2 = H_2$ in the Eq. (2)) and water vapor, the electrode reactions include:

$$H_{2(g)} \Leftrightarrow 2H^+ + 2e^- \tag{10}$$

and

$$H_2O_{(g)} + 2e^- \Leftrightarrow H_{2(g)} + O^{2-} \tag{11}$$

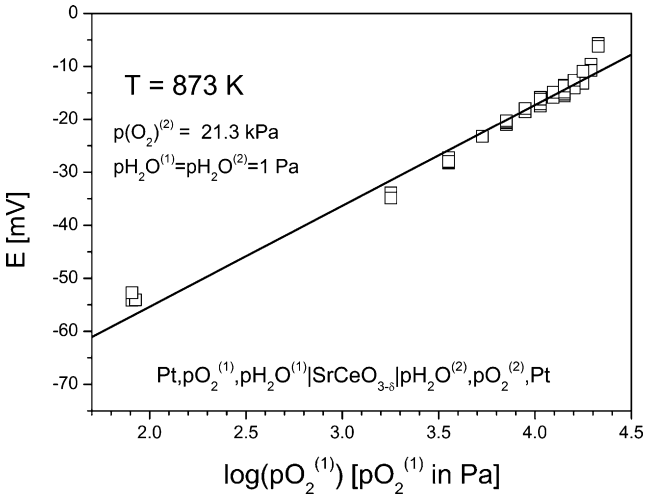

Fig. 7. The example results of measured E vs. pH_2 for the cells made from $SrCeO_{3-\delta}$ at 773 K.

Integrating Eq. (3) we have:

$$E = \frac{RT}{2F}\left(t_O \ln\frac{pH_2O^{(2)}}{pH_2O^{(1)}} - (t_O + t_H)\ln\frac{pH_2^{(2)}}{pH_2^{(1)}}\right) \quad (12)$$

Taking into consideration Eq. (8) we have:

$$E = -\frac{RT}{2F}(t_O + t_H)\ln\frac{pH_2^{(2)}}{pH_2^{(1)}} \quad (13)$$

Fig. 8 shows the example results of measured E as a function of pH_2 at 773 K for $SrCeO_{3-\delta}$ solid electrolyte. The ionic transference numbers ($t_O + t_H$) were determined from the linear approximation of the experimental points.

Fig. 9 shows the example dependence of ionic transference numbers as a function of temperature for the $SrCeO_{3-\delta}$ sample. As can be seen, ionic transference numbers assume values above 0.50–0.60 at temperature range 500–650 °C. Above this temperature range the decrease of ionic transference number with

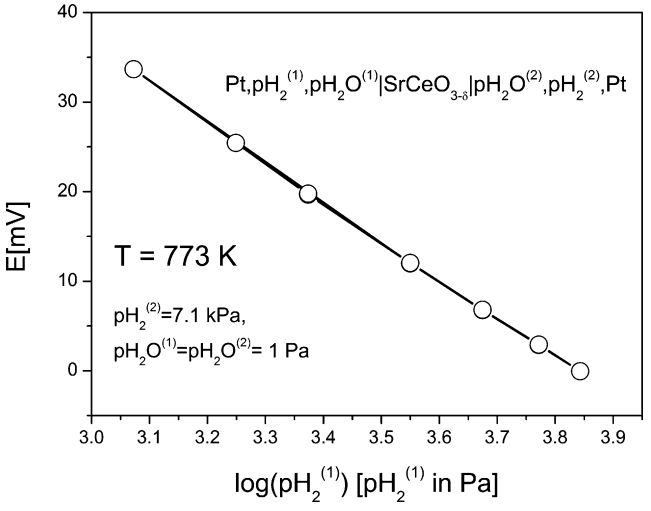

Fig. 8. The example results of measured E vs. pO_2 for the cells made from $SrCeO_{3-\delta}$ at 873 K.

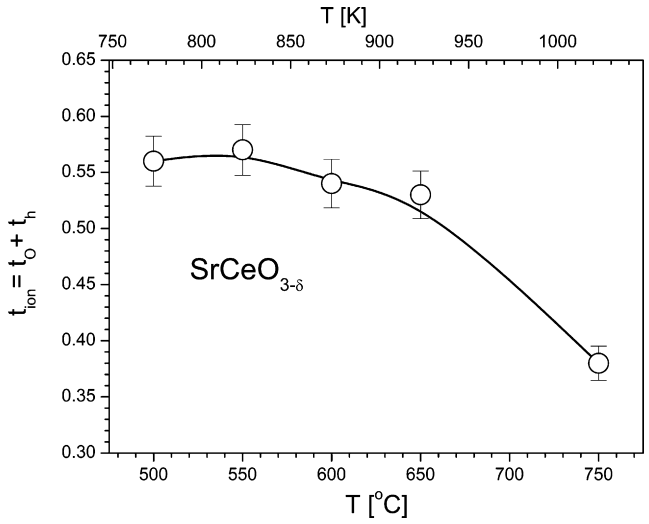

Fig. 9. The dependence of ionic transference numbers as a function of temperature for the $SrCeO_{3-\delta}$ sample.

temperature is observed. It can be explained by thermal decomposition of the protonic defects. It remains in agreement with literature report that at high temperatures in dry atmospheres water is desorbed, resulting in disappearance of protonic defects and formation of less mobile oxygen vacancies [23]. Moreover, interaction of the solid material with gas atmosphere observed at high temperatures leads to increase of electronic charge carriers (electrons or electron holes at low or high pO_2, respectively). This process causes increase of the electronic transference numbers and simultaneous decrease of ionic transference numbers.

4. Conclusions

The results of XRD, SEM and EIS measurements presented in this paper indicate the strong influence of Y dopant on the properties of studied materials. The used preparation method (solid state reaction) leads to dense samples with uniform grain sizes with 3–5 μm of diameter. The materials show perovskite rhombohedral structure. The XRD measurements and SEM observations of samples allowed determining the solubility limit of yttrium in the $SrCeO_3$ lattice; the $SrCeO_3$ and Y_2O_3 form homogenous solid solutions up to 5% mol. of Y dopant. The lattice parameters change with Y content according to substitutional mechanism of incorporation yttrium ions into cerium sublattice. The preliminary results of electrochemical impedance spectroscopy (EIS) measurements performed as a function of temperature and gas atmosphere composition lead to determining the total electrical conductivity of the materials. Electrical conductivity include ionic (both proton and oxygen ion components) and electronic component. Below 10^{-15} Pa materials are the n-type semiconductor, whereas above 10^2 Pa the p-type conductivity is predominant. EIS measurements allowed determining grain boundary and bulk electrical conductivities and their activation energies. The potentiometric EMF measurements of the cells composed of $SrCeO_{3-\delta}$-based solid electrolytes allowed to determine the ionic transference numbers. The high transference numbers for ionic defects (ca.

0.5–0.6) were found in the temperature range of 500–650 °C. Above the 650 °C the decrease of ionic transference number was observed.

In spite of the high ionic conductivity, doped $SrCeO_3$-based materials have not been commercialized to date due to its poor thermodynamic stability under real operating environments (e.g. reaction with CO_2, the major constituent of the gas mixture from which H_2 is to be separated). On the other hand observed mixed conductivity in studied materials gives opportunity to use them as electrode materials in fuel cells (in order to extend three phase boundary) [24], especially operating at intermediate temperatures. Also, there is potential possibility to apply these materials in hydrogen permeable membranes in hydrogen technology [25].

We believe that the weak corrosion resistance against the CO_2 may be reduced in the case of saturated $SrCeO_3$–Y_2O_3 solid solutions. Further works are under the way in order to investigate the influence of additional phase on stabilization of material properties.

Acknowledgments

The financial support of Polish Ministry of Education and Science (MEiN), Project No. 3 T08D 049 29 is acknowledged.

References

[1] H. Iwahara, T. Esaka, H. Uchida, N. Maeda, Solid State Ionics 34 (1981) 359.
[2] T. Norby, Solid State Ionics 125 (1999) 1.
[3] K.D. Kreuer, Chem. Mater. 8 (1996) 610.
[4] M. Pionke, T. Mono, W. Sweika, T. Springer, H. Schober, Solid State Ionics 97 (1997) 497.
[5] R. Hempelmann, M. Soetratmo, O. Hartmann, R. Waeppling, Solid State Ionics 107 (1998) 269.
[6] K.D. Kreuer, W. Muench, U. Traub, J. Maier, Ber. Bunsenges. Phys. Chem. 102 (1998) 552.
[7] F. Shimojo, K. Hashino, H. Okazaki, J. Phys. Soc. Jpn. 66 (1997) 8.
[8] T. Norby, Solid State Ionics 40/41 (1990) 849.
[9] P. Colomban, Ann. Chim. Sci. Mat. 24 (1999) 1.
[10] T. Schreban, A.S. Nowick, Solid State Ionics 35 (1989) 189.
[11] H. Uchida, N. Maeda, H. Iwahara, Solid State Ionics 11 (1983) 117.
[12] J. Nowotny, M. Rekas, Ceram. Int. 20 (1994) 257.
[13] H. Iwahara, Solid State Ionics 86–88 (1996) 9.
[14] N. Bonanos, Solid State Ionics 53/56 (1992) 967.
[15] T. Yaima, H. Iwahara, Solid State Ionics 50 (1992) 281.
[16] K.S. Knight, N. Bonanos, Mater. Res. Bull. 30 (3) (1995) 347.
[17] I. Kosacki, J.G.M. Becht, R. van Landschoot, J. Schoonman, Solid State Ionics 59 (1993) 287.
[18] J.F. Liu, A.S. Nowick, Solid State Ionics 50 (1992) 131.
[19] H.M. Rietveld, J. Appl. Crystallogr. 2 (1969) 65–71.
[20] R.J. Phillips, N. Bonanos, F.W. Poulsen, E.O. Ahlgren, Solid State Ionics 125 (1999) 389.
[21] T. van Dijk, A.J. Burggraaf, Phys. Stat. Sol. (a) 63 (1981) 229, and Ref. 1–7 herein.
[22] A.R. Potter, R.T. Baker, Solid State Ionics 177 (2006) 1917, and Ref. 1 & 9 herein.
[23] e.g. V.V. Kharton, I.P. Marozau, G.C. Mather, E.N. Naumovich, J.R. Frade, Electrochim. Acta 51 (2006) 6389.
[24] N.Q. Minh, J. Am. Ceram. Soc. 76 (1993) 563.
[25] H. Iwahara, Y. Asakura, K. Katahira, M. Tanaka, Solid State Ionics 168 (2004) 299.